2013

Coded apertures for x-ray scatter imaging

David J. Brady
Duke University

Daniel L. Marks
Duke University

Kenneth P. MacCabe
Duke University

Joseph A. O'Sullivan
Washington University School of Medicine in St. Louis

Coded apertures for x-ray scatter imaging

David J. Brady,[1,*] Daniel L. Marks,[1] Kenneth P. MacCabe,[1] and Joseph A. O'Sullivan[2]

[1]Fitzpatrick Institute for Photonics and Department of Electrical and Computer Engineering, Duke University, P.O. Box 90291, Durham, North Carolina 27708, USA

[2]Departments of Radiology and Electrical Engineering, Washington University, Box 1127, St. Louis, Missouri 63130, USA

*Corresponding author: dbrady@duke.edu

Received 26 July 2013; revised 27 September 2013; accepted 4 October 2013; posted 4 October 2013 (Doc. ID 194672); published 7 November 2013

We examine coding strategies for coded aperture scatter imagers. Scatter imaging enables tomography of compact regions from snapshot measurements. We present coded aperture designs for pencil and fan beam geometries, and compare their singular value spectra with that of the Radon transform and selected volume tomography. We show that under dose constraints scatter imaging improves conditioning over alternative techniques, and that specially designed coded apertures enable snapshot 1D and 2D tomography. © 2013 Optical Society of America

OCIS codes: (110.7440) X-ray imaging; (340.7430) X-ray coded apertures; (110.1758) Computational imaging.

http://dx.doi.org/10.1364/AO.52.007745

1. Background

The focus of this paper is tomography based on coded aperture x-ray scatter imaging (CAXSI). We consider pencil and fan beam geometries, and use singular value decomposition (SVD) to compare each CAXSI system with other tomographic strategies, such as Radon imaging and selected volume tomography (SVT). Singular value analysis is often used to evaluate the noise sensitivity of measurement systems and to quantify the number of components measured above the noise floor. We show that the singular values for CAXSI decay more slowly compared with other techniques as the image resolution is increased. Pencil beam CAXSI enables imaging along a single ray from a snapshot measurement (a single exposure of a detector array) by detecting a diversity of scattered x rays [1]. Fan beam CAXSI enables snapshot imaging within a plane normal to a 2D detector array [2]. Careful selection of scattered rays could be important for minimizing radiation doses and/or maximizing throughput in tomographic systems.

Scatter imaging was first proposed in 1959 [3] and has been the subject of numerous studies and reviews [4]. Scatter tomography has used Radon methods [5] and energy resolved detection [6]. The most common strategy, however, relies on SVT using collimation filters at the source and at the detector [7]. CAXSI is a novel approach to scatter imaging that uses coded masks between the scattering object and the detector array. In contrast with collimation filters, the coded aperture allows rays from multiple directions to simultaneously illuminate each detector pixel. Increased photon efficiency is the advantage of CAXSI relative to selected volume imaging.

Following initial proposals for spectroscopy [8] and imaging [9], coded aperture optical systems focused for many years on Hadamard codes for spectroscopy [10] and uniformly redundant arrays for imaging [11]. Recent studies, however, show that novel codes in combination with biased, nonlinear, and/or decompressive estimators may achieve comparable or better results [12]. As an example, coded aperture snapshot spectral imaging uses pseudorandom codes

1559-128X/13/327745-10$15.00/0

to improve the efficiency of spectral image collection [13]. For sparse or compressible objects coded aperture multiplexing can improve system sensitivity and SNR even when photon noise is dominant [14].

The system geometry for forward scatter CAXSI is illustrated in Fig. 1. Scattered radiation from an illuminated sample passes through a coded aperture placed a distance d in front of a 2D detector array. CAXSI owes its throughput and snapshot advantages to the combination of scatter imaging and coded apertures with high transmittance (50%), a number of which are presented in this paper. An ideal coded aperture will minimize self-similarity under translation, scaling, and/or rotation. Specifically, a shift (translation) code $t(x)$ will possess a correlational inverse $\hat{t}(x)$ such that $\int t(x)\hat{t}(x-a)\mathrm{d}x = \delta(a)$, where $\delta(\cdots)$ is the Dirac delta function. For a scale code, $\int t(x)\hat{t}(xa)\mathrm{d}x = \delta(a-1)$. Similar conditions can be constructed for rotational codes. For incoherent imaging, $0 \le t(x) \le 1$ but $\hat{t}(x)$ is not bound by this constraint since it is applied digitally.

Shift codes are well known in coded aperture imaging and provide resolution parallel to a detector array. The shift codes in this paper are based on quadratic residues. We motivate the use of harmonic functions as scale codes due to their distinguishability under magnification, providing resolution in range from a detector plane. We present combined scale and rotation codes for pencil beam illumination providing resolution in both range and scattering angle. For fan beam illumination, we combine scale and shift codes to image planes perpendicular to the detector array.

In this paper, linear scattering models are analyzed which are applicable when attenuation is negligible or otherwise corrected for. We derive analytic SVDs for isotropic scattering objects and resort to numerical evaluation for the anisotropic cases. SVD may be performed for any linear operator over continuous or discrete domains and provides a powerful tool for comparing measurement systems. Reference [12] discusses SVD analysis for computational imaging and related reconstruction methods, such as truncated SVD and Tikhonov regularization. The fundamental concept is that measurement noise produces an effective singular value cutoff below which the singular vectors are not reliably recovered.

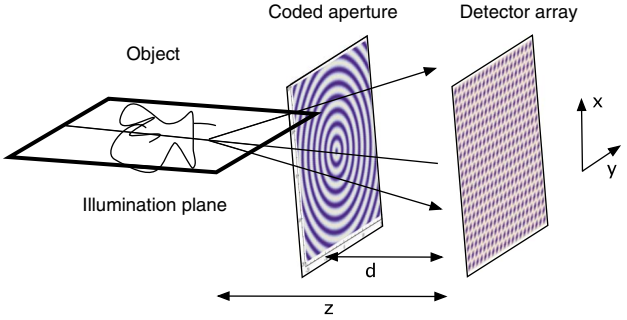

Fig. 1. System geometry for planar scatter imaging.

The next section analyzes pencil beam CAXSI under the assumption of isotropic scattering. This is extended to anisotropic scattering and applicable coded aperture designs are presented in Section 3. A coded aperture for fan beam illumination and isotropic scattering is presented in Section 4, and the scalability of CAXSI is compared with other tomographic strategies in Section 5. Results are summarized in Section 6.

2. Pencil Beam CAXSI

As a first example of code design, suppose that a pencil beam illuminates a section of the target object distributed along the z axis. Our goal is to image object scattering density $f(x=0,y=0,z)$. The full volume may subsequently be reconstructed by raster scanning.

We assume isotropic scatter to all detector positions, which approximates Compton (incoherent) scattering or x-ray fluorescence when attenuation is weak and the detector array subtends a small solid angle with respect to the object (this assumption will be relaxed in Section 3). The detector elements lie in the $z=0$ plane and measure the scatter. The scatter visibility is modulated by a coded aperture a distance d from the detector plane. For simplicity, we assume a 1D coded aperture transmittance $t(x)$, where x may be a Cartesian coordinate or a radius from the pencil beam axis. The signal at coordinate x in the detector plane is

$$g(x) = \int_d^{z_{\max}} f(z)t\left[x\left(1-\frac{d}{z}\right)\right]\mathrm{d}z. \tag{1}$$

For simplicity, the system geometric response is omitted and the source is monochromatic. Estimation of $f(z)$ from $g(x)$ is enabled by judicious selection of $t(x)$.

The coordinate transformation $\beta = 1-d/z$ changes Eq. (1) to

$$g(x) = \int_0^1 \tilde{f}(\beta)t(x\beta)\mathrm{d}\beta, \tag{2}$$

where $\tilde{f}(\beta) = f(z=d/(1-\beta))d/(1-\beta)^2$ and we assume $z_{\max} \gg d$. Equation (2) is a "scale transformation"; inversion is straightforward if $t(x)$ is orthogonal in scale.

Harmonic functions are orthogonal in scale (sinusoids at different frequencies have vanishing correlation). The simplest choice for $t(x)$ satisfying the requirements that $0 \le t \le 1$ is $t(x) = [1-\cos(2\pi ux)]/2$, where u is the spatial frequency of the coded aperture. The measurement model is then

$$g(x) = \frac{1}{2}\int_0^1 \tilde{f}(\beta)[1-\cos(2\pi ux\beta)]\mathrm{d}\beta. \tag{3}$$

Equation (3) is familiar as the forward model for the Fourier transform spectroscopy [12]. The singular

vectors for this transformation are derived from the constant singular vector associated with the **1** operator and prolate spheroidal singular vectors associated with the kernel $\cos(2\pi ux\beta)$. Assuming that the support of $g(x)$ is $[0,X]$, the singular value corresponding to the first operator is $N_x = uX$, which is the number of harmonic periods that are observed for a scatter point at $z = \infty$.

The singular vectors of the operator $-(1/2)\cos 2\pi ux\beta$ supported over $\beta \in [0,1]$ and $x \in [0,X]$ are the prolate spheroidal wave functions $\psi_n(\beta)$ for n even [15]. The corresponding singular values are $\sqrt{\lambda_n N_x/2}$, where $\lambda_n \approx 1$ for $n < N_x/2$ and $\lambda_n \approx 0$ for $n > N_x/2$ [12].

The even prolate spheroidal functions are not orthogonal to the constant vector over [0, 1] but the much larger singular value associated with the constant vector means that the spaces spanned by the two operators approximate the space spanned by their sum. The singular decomposition space thus consists of a single vector with singular value $N_x/2$ and $N_x/2 - 1$ secondary vectors corresponding to singular values $\sqrt{N_x}/2$.

The prolate spheroidal basis yields resolution elements of length $1/N_x$ distributed uniformly distributed over $\beta = [0,1]$. Converting back to the z coordinate, one derives resolution

$$\Delta z = \frac{z^2}{N_x d}. \tag{4}$$

This expression may be understood by noting that the location z of a single point scatterer is localized by observing u', the frequency of the sinusoid projected onto the detector. The aperture code is magnified by a factor $z/(z-d)$ and so $u' = u(z-d)/z$. The signals from two point scatters separated by a distance Δz lose orthogonality when $\Delta u' \le u/N_x$ due to the finite detector size. Propagating this uncertainty to z through $\Delta u' = (\partial u'/\partial z)\Delta z$ produces Eq. (4).

3. Anisotropic Scattering

In the previous section we motivated the use of harmonic codes for range discrimination under isotropic scattering. If a 2D detector is used, there is a redundancy of scattered rays, which may be exploited to estimate features other than density along the 1D object. In this section we present such an example where a more general scattering model relaxes the assumption of isotropic scattering to allow dependence on θ, the polar scattering angle. This applies, for instance, to Bragg (coherent) scattering from liquids, powders, and amorphous compounds. In this case one may vary the code $t(\varphi,\rho)$ as a function of angle φ and radius ρ in order to image θ and z simultaneously. The forward model in this case is

$$g(\varphi,\rho) = \int_d^{z_{\max}} f(z,\theta)\, t\left[\varphi, \rho\left(1 - \frac{d}{z}\right)\right] \mathrm{d}z \tag{5}$$

with polar angle φ and radius ρ in the detector plane. Let $r = \rho(1 - (d/z))$ be the radius at which the ray connecting beam position z with detector radius ρ intersects the aperture plane. Transforming the integral in Eq. (5) from z to r, and defining $f(r,\rho) = (\rho d/(\rho - r)^2) f(z = \rho d/(\rho - r), \theta = \tan^{-1}(\rho - r/d)$, the forward model takes the simple form

$$g(\varphi,\rho) = \int t(\varphi,r) f(r,\rho)\mathrm{d}r. \tag{6}$$

Each radius therefore defines a subspace for the operator $\int t(\varphi,r)(\cdots)\mathrm{d}r$ and its matrix representation $\mathbf{t}$. The elements of $\mathbf{t}$ are $t_{ij} = t(i\Delta\varphi, j\Delta r)$, given by samples of the transmittance at regular intervals in φ and r. Because $\mathbf{t}$ operates on subspaces, the singular values of Eq. (6) are equal to those of $\mathbf{t}$. However, the transformation from $(z,\theta) \to (r,\rho)$ is not unitary and therefore the SVD of Eq. (5) is more complicated, motivating numerical evaluation.

We seek invertible codes for $\mathbf{t}$ with entries in [0, 1]. The simplest coded aperture is based on the identity matrix, shown in polar and Cartesian coordinates in Fig. 2. This aperture is a type of collimator since each detector receives a single ray, and therefore provides minimal throughput. Multiplexing with 50% average transmittance can be achieved by a coded aperture based on a discrete cosine transform (DCT), shown in Fig. 3. This mask contains gray scale values, but some applications require binary codes due to fabrication limitations. This motivates codes based on a Hadamard matrix (Fig. 4) or randomized features (Fig. 5). A high-resolution Cartesian image of the DCT code is included, which shows its continuous form, and the columns of the Hadamard matrix have been sorted so the angular frequency increases with radius. This sorting operation is unitary and therefore preserves the singular value spectrum.

For each of the apertures in Figs. 2–5, the forward model from Eq. (5) was numerically simulated as a matrix in order to find its singular value spectrum. The object was sampled with 48×48 pixels from $z = d$ to $2d$ and $\theta = 0$ to 27°. Each coded aperture was simulated at $d = 100$ mm with 31 polar sections and 31 radial sections from $r = 0$ to 25 mm. The detector was sampled with 96 polar and 96 radial sections from $\rho = 0$ to 50 mm. The singular value spectra for these code choices are plotted together in Fig. 6, and we have included the harmonic code $t(x)$, which was previously derived for isotropic scattering. The identity code shows the poorest performance, due to its low overall transmission. The harmonic and DCT codes show significantly larger values and follow each other closely. The Hadamard and random binary codes have the largest singular values and choosing between these two depends on which singular vectors should be emphasized.

4. Fan Beam CAXSI

CAXSI may also be applied to planar imaging. Once again, we consider isotropic scattering for simplicity.

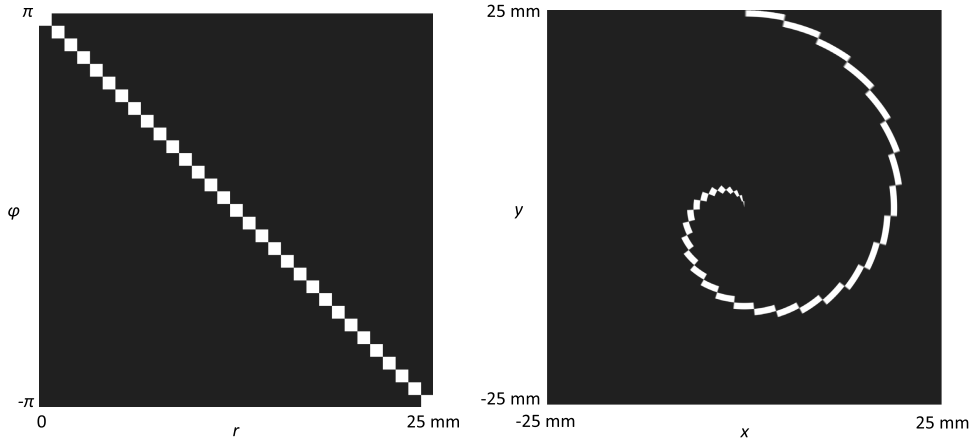

Fig. 2. Coded aperture based on the identity matrix. (a) Polar coordinates (r, φ). (b) Cartesian coordinates (x,y).

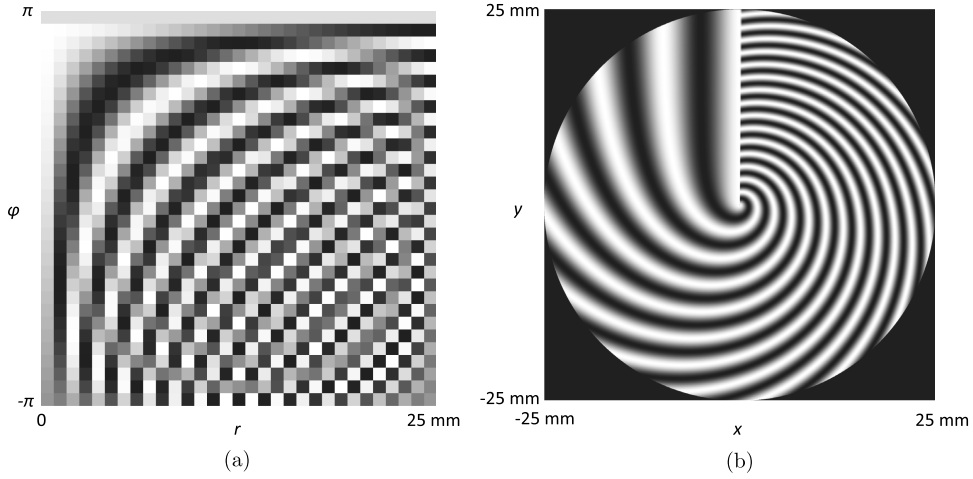

Fig. 3. Coded aperture based on the DCT. (a) Polar coordinates (r, φ). (b) Cartesian coordinates (x,y).

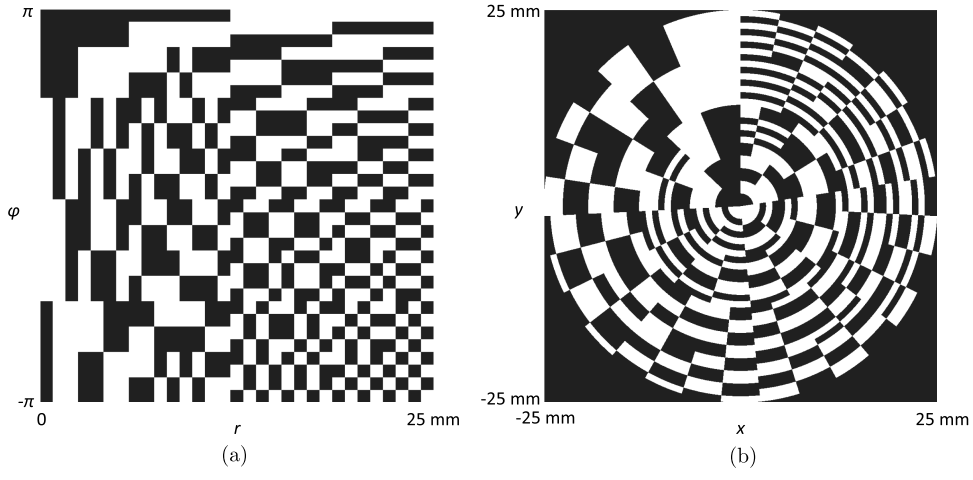

Fig. 4. Coded aperture based on a Hadamard matrix. (a) Polar coordinates (r, φ). (b) Cartesian coordinates (x,y).

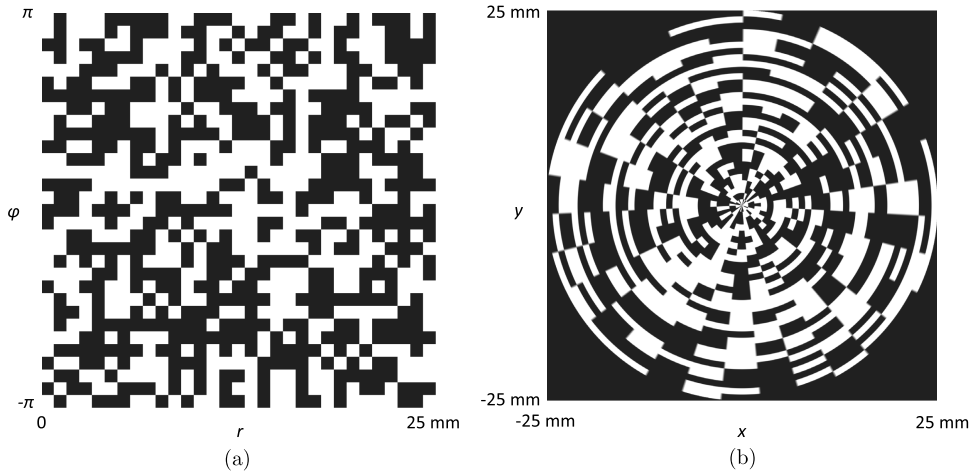

Fig. 5. Coded aperture based on a random binary matrix. (a) Polar coordinates (r, φ). (b) Cartesian coordinates (x, y).

When the entire y–z plane is illuminated as in Fig. 1, the forward model becomes

$$g(x,y) = \int_{-Y/2}^{Y/2} \int_{d}^{z_{\max}} f(x'=0, y', z') \times t\left[x\left(1-\frac{d}{z'}\right), y\left(1-\frac{d}{z'}\right) + y'\frac{d}{z'}\right] \mathrm{d}y' \mathrm{d}z'. \quad (7)$$

Choosing $t(x,y) = [1 + \sin(2\pi u x) p(\nu y)]/2$ where $p(\nu y)$ is orthogonal in translation provides sensitivity to shifts in y and z. The quantity ν is the spatial frequency of the code in the y direction. We assume specifically that

$$p(y) = \sum_n p_n [2\,\mathrm{rect}(y-n) - 1],$$

where $\mathrm{rect}(y)$ is a unit square pulse of width 1 and $\{p_n\}$ is a binary sequence with two-level autocorrelation. Such sequences may be found for various code lengths [16]. Quadratic residue derived codes of length $P = 4m + 1$, with P prime, are particularly straightforward, and yield transverse imaging resolution $\Delta y = z/(\nu d)$ [11]. Two scatter points separated by Δy produce signals shifted by one code period in the y direction.

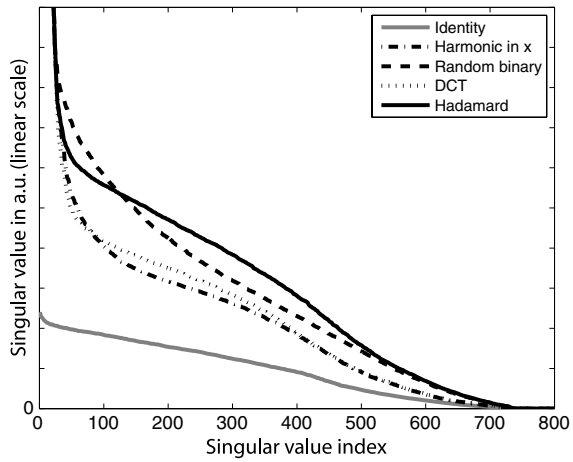

Fig. 6. Singular value spectra of the pencil beam system for each code choice.

Figure 7 shows aperture designs that are harmonic in the horizontal (x) axis and translation coded in the vertical (y) axis using quadratic residue codes. The aperture resolution (number of code features) was varied separately in each direction to illustrate the scaling of the singular value spectrum, shown in Fig. 8. Measurements were numerically simulated over a 100 mm × 100 mm area and 96 × 96 samples. The object was represented by 48 × 48 pixels over a square region of dimension 100 mm in the y–z plane, centered 150 mm from the detector. The coded aperture was simulated at distance 100 mm from the detector and tiled to provide full coverage from all scatter points.

A look at the singular value spectra in Fig. 8 reveals the effect of code resolution. The codes with 16 features (eight sinusoid periods) in the x direction both cutoff at about 900 singular values, and the codes with 32 features in x retain about 1600 singular values. Increasing the shift code resolution from 17 to 29 features amplifies the singular values but does not appear to add more. Increasing the frequency of the harmonic code has the strongest effect of adding singular values and amplifying the spectrum.

The coded aperture with 32 × 29 features was compared with a similar random code drawn from a uniform distribution on [0, 1], shown in Fig. 9. The singular value spectra for the CAXSI systems using the two codes are shown in Fig. 10. For the first 620 singular values our code outperforms the random code but then a crossover occurs and the random code produces a more slowly decaying spectrum. We expect the random aperture will perform worse in a noisy environment where a limited number of singular vectors are measurable.

5. Scalability of Imaging Techniques

In this section we compare Radon imaging and SVT with CAXSI for 2D tomography under the constraint

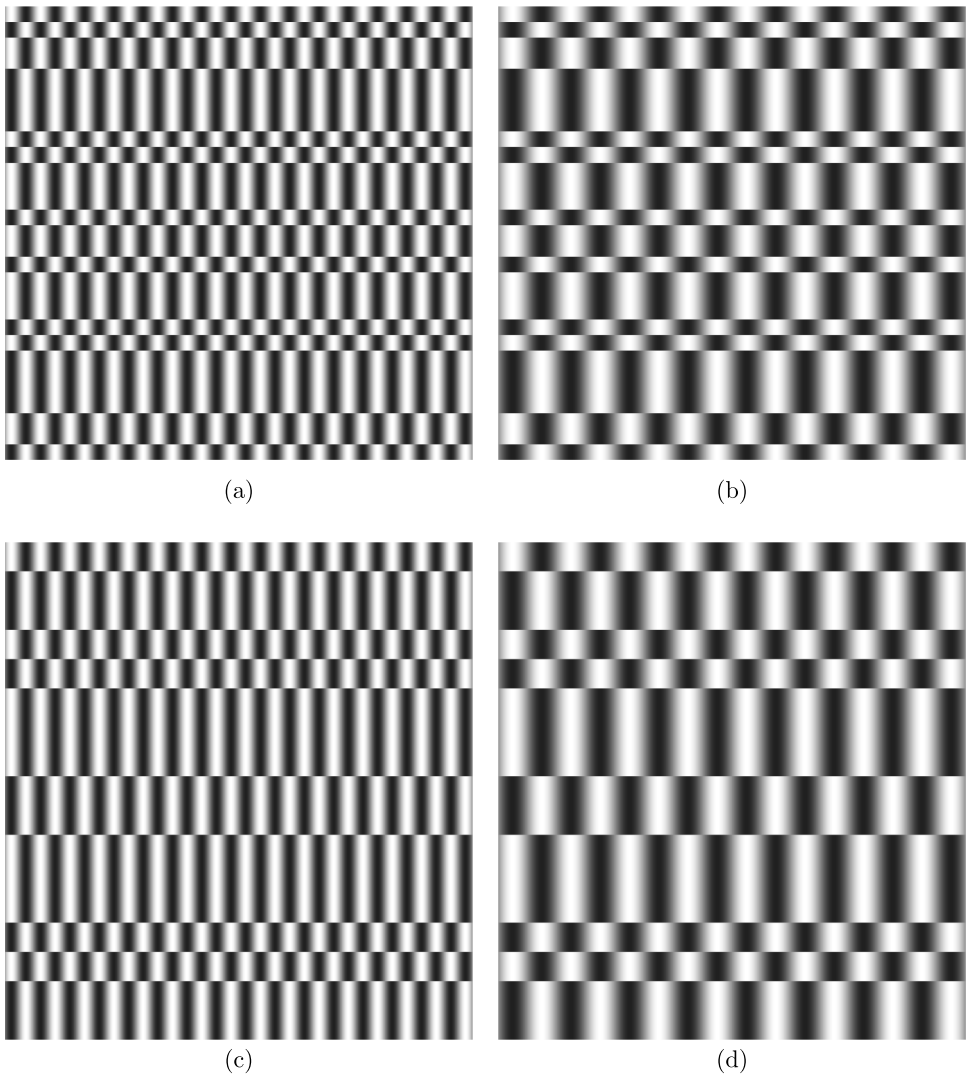

Fig. 7. Coded apertures based on a sinusoid in x (horizontal) and a quadratic residue in y (vertical). The number of code features in each direction (x,y) are (a) 32×29, (b) 16×29, (c) 32×17, and (d) 16×17 features.

of fixed radiation dose. The singular values for each technique scale with the resolution of the desired image, where we assume the number of measurements

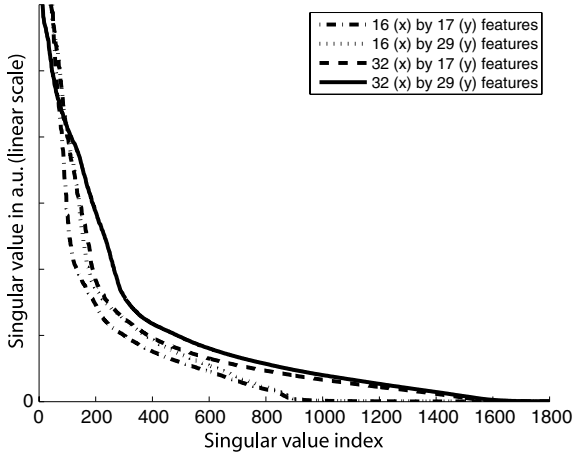

Fig. 8. Singular value spectra for each of the coded apertures in Fig. 7.

M equals the number of object coefficients. Radon imaging is a method of transmission tomography where the measurements are line integrals of the target's density. Radon imaging requires multiple exposures for each tomographic image. The singular values of the 2D Radon transform are $\lambda_m = \sqrt{4\pi/(m+1)}$ [17], with each value having a degeneracy of $m+1$. The Radon transform therefore yields typical singular values proportional to $1/M^{1/4}$. Letting N be the number of reconstructed pixels in each object dimension, $M = N^2$ so the singular values are of magnitude $1/\sqrt{N}$. A pencil beam scanned over a plane produces N subspaces each with N singular values proportional to $1/\sqrt{N}$. For the Radon system to deliver the same dose as the scanned pencil beam, the source must be N times dimmer during Radon's N exposures. The effective scaling is then $1/N^{3/2}$ for Radon and $1/\sqrt{N}$ for pencil beam CAXSI. In Appendix A, we show that the singular values scale like $1/N$ for fan beam CAXSI, and since this is a snapshot technique the dose is comparable to the scanned pencil beam.

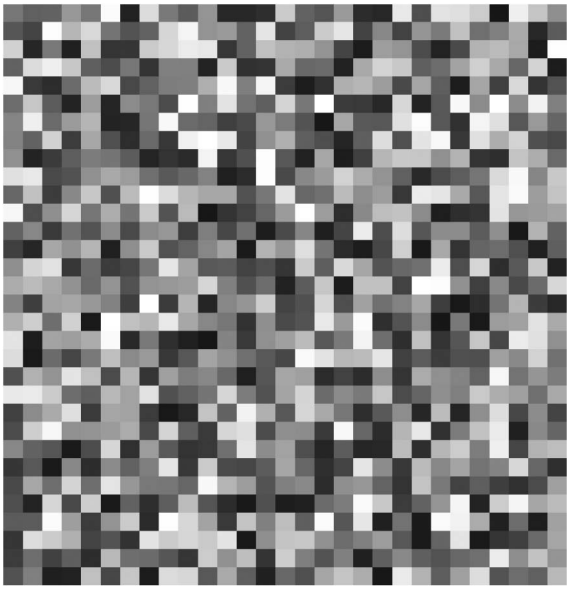

Fig. 9. Coded aperture with resolution 32 × 29 based on uniform random values in [0, 1].

SVT is a scatter imaging technique that uses collimation at the source and detector so that each measurement is sensitive to a single object voxel [7]. Using an array of detectors collimated appropriately, snapshot measurement is possible using SVT. The measurement matrix for SVT is diagonal and the elements are the singular values. For a fixed dose, the singular values are proportional to $1/N$ for a pencil beam and $1/N^2$ for a fan beam since these are the fractions of voxels contributing to each measurement.

Table 1 summarizes the scaling laws for 1D and 2D imaging using pencil and fan beam CAXSI, Radon imaging, and SVT. In each case the singular values are scaled so the maximum is 1. Both pencil and fan beam CAXSI show improvement over other methods for 1D and 2D imaging. In addition, pencil beam CAXSI enables independent reconstruction of each ray, whereas planar Radon imaging multiplexes

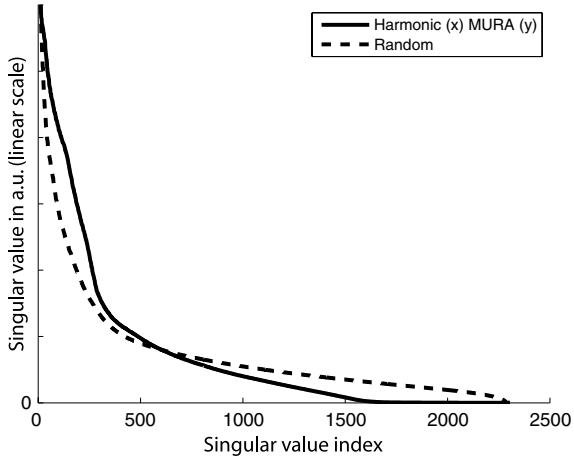

Fig. 10. Singular value spectra for the proposed code and a random code.

Table 1. Scaling of Dose-Constrained Singular Values for Pencil Beam CAXSI, Fan Beam CAXSI, Radon Imaging, and SVT[a]

Image Dimension	Pencil	Fan	Radon	SVT
1D	$1/\sqrt{N}$	—	—	$1/N$
2D	$1/\sqrt{N}$	$1/N$	$1/N^{3/2}$	$1/N^2$

[a]In each case the singular values are scaled so that the maximum is 1.

points over a plane. Independent reconstruction of each subspace enables spot tomography, where a single pencil beam illuminates a region of interest, eliminating unnecessary doses to neighboring regions.

These results assume equal photon efficiency for scatter and transmission imaging. In practice, the scatter systems will include an additional factor for the fraction of the total scatter signal detected, and the ratio of scattered to transmitted photons for the object of interest.

6. Summary

In this paper, we present CAXSI techniques employing pencil and fan beam illumination. By using specially designed coded apertures, 1D and 2D density distributions can be reconstructed from a single exposure of an appropriate imaging detector. Harmonic codes are shown to provide range resolution under the assumption of isotropic scattering, an approximation for x-ray fluorescence and Compton (incoherent) scattering. Two-dimensional codes are developed for anisotropic scattering along a pencil beam, applicable to Bragg scattering from liquids, powders, and amorphous compounds. For each system we present singular value analyses of the first-order scattering model, which are compared with Radon imaging under a fixed dose constraint. CAXSI shows several advantages, including improved scalability, snapshot capability, and the prospect of "spot tomography" where isolated regions of interest are irradiated. Further refinement of the scattering models will include energy-dependent absorption and multiple scattering effects, as well as energy-sensitive measurement techniques. Improved performance is expected when scatter and transmission signals are used together in joint estimation of object structure.

Appendix A

In this section we derive the SVD for fan beam CAXSI. Starting with the forward model in Eq. (7), we introduce the projective coordinates:

$$\alpha = y' \frac{d}{z'}$$

$$\beta = 1 - \frac{d}{z'}.$$

If we define a new object function $F(\alpha, \beta) = (d/(1-\beta)^3) f(x' = 0, (\alpha/1-\beta), (d/1-\beta))$, the forward model becomes

$$g(x,y) = \int_0^1 \int_{-\infty}^{\infty} F(\alpha,\beta) t[x\beta, \beta y + \alpha] \mathrm{d}\alpha \mathrm{d}\beta.$$

The adjoint is defined by

$$F_A(\alpha',\beta') = \int_{-Y/2}^{Y/2} \int_{-X/2}^{X/2} g(x,y) t[x\beta', \beta' y + \alpha']^* \mathrm{d}x \mathrm{d}y.$$

We rearrange this expression in terms of the normal operator:

$$F_A(\alpha',\beta') = \int_0^1 \int_{-\infty}^{\infty} F(\alpha,\beta) K(\alpha,\beta,\alpha',\beta') \mathrm{d}\alpha \mathrm{d}\beta$$

with kernel function

$$K(\alpha,\beta,\alpha',\beta') = \int_{-X/2}^{X/2} \int_{-Y/2}^{Y/2} t[x\beta, \beta y + \alpha] \times t[x\beta', \beta' y + \alpha']^* \mathrm{d}x \mathrm{d}y. \quad \text{(A1)}$$

Now consider a separable aperture code with the form $t(x,y) = [1 + A(x)B(y)]/2$ and $-1 \le A(x) B(y) \le 1$. Inserting this into Eq. (A1),

$$K_S(\alpha,\beta,\alpha',\beta') = \int_{-X/2}^{X/2} \int_{-Y/2}^{Y/2} \frac{1 + A(x\beta) B[\beta y + \alpha]}{2} \times \frac{1 + A(x\beta')^* B[\beta' y + \alpha']^*}{2} \mathrm{d}y \mathrm{d}x.$$

We consider codes with 50% average transmission so that $\int_{-X/2}^{X/2} \int_{-Y/2}^{Y/2} A(x\beta) B[\beta y + \alpha] \mathrm{d}y \mathrm{d}x \approx 0$. Then we can neglect this contribution and consider only

$$K_S(\alpha,\beta,\alpha',\beta') = \frac{XY}{4} + \frac{1}{4} \int_{-X/2}^{X/2} A(x\beta) A(x\beta')^* \mathrm{d}x \times \int_{-Y/2}^{Y/2} B[\beta y + \alpha] B[\beta' y + \alpha']^* \mathrm{d}y. \quad \text{(A2)}$$

With our scale code $A(x) = \cos(2\pi u x)$, the integral over X is

$$\begin{aligned} &\int_{-X/2}^{X/2} \cos(2\pi u x \beta) \cos(2\pi u x \beta') \mathrm{d}x \\ &= \frac{1}{2} \int_{-X/2}^{X/2} \cos[2\pi u x(\beta - \beta')] + \cos[2\pi u x(\beta + \beta')] \mathrm{d}x \\ &= \frac{1}{2\pi u(\beta - \beta')} \sin[\pi u X(\beta - \beta')] \\ &\quad + \frac{1}{2\pi u(\beta + \beta')} \sin[\pi u X(\beta + \beta')] \\ &\approx \frac{X}{2} \mathrm{sinc}[N_x(\beta - \beta')] \end{aligned}$$

with $N_x = uX$. This neglects the rapidly oscillating term $\beta + \beta'$. The eigenfunctions for the sinc kernel are the prolate spheroidal wave functions [18]; however, we take a different approach here. For simplicity we take $N_x \gg 1$ so that the integral is only nonzero when $\beta \approx \beta'$. Equation (A2) is approximated by

$$K_S(\alpha,\beta,\alpha',\beta') = \frac{XY}{4} + \frac{X}{8} \mathrm{sinc}[N_x(\beta - \beta')] \times \int_{-Y/2}^{Y/2} B\left[\frac{\beta + \beta'}{2} y + \alpha\right] B\left[\frac{\beta + \beta'}{2} y + \alpha'\right]^* \mathrm{d}y$$

with $(\beta + \beta'/2) \approx \beta \approx \beta'$ at the peak of the sinc function. If $B(y)$ is periodic with period P so that $B(y) = \sum_{n=-\infty}^{\infty} c_n \exp(2\pi i n y/P)$ (as would be represented by a convolutional code), then

$$K_S(\alpha,\beta,\alpha',\beta') = \frac{XY}{4} + \frac{X}{8} \mathrm{sinc}[N_x(\beta - \beta')] \times \int_{-Y/2}^{Y/2} \left[\sum_n c_n \exp\left(\frac{2\pi i n}{P}\left[\frac{\beta + \beta'}{2} y + \alpha\right]\right)\right] \times \left[\sum_{n'} c_{n'}^* \exp\left(\frac{-2\pi i n'}{P}\left[\frac{\beta + \beta'}{2} y + \alpha'\right]\right)\right] \mathrm{d}y.$$

We approximate the integral with a full period over the periodic function, which is $2P/\beta + \beta'$, neglecting any edge effects:

$$\begin{aligned} &K_S(\alpha,\beta,\alpha',\beta') \\ &= \frac{XY}{4} + \frac{X}{8} \mathrm{sinc}[N_x(\beta - \beta')] \frac{Y(\beta + \beta')}{2P} \\ &\quad \times \int_{-P/(\beta+\beta')}^{P/(\beta+\beta')} \left[\sum_n c_n \exp\left(\frac{2\pi i n}{P}\left[\frac{\beta + \beta'}{2} y + \alpha\right]\right)\right] \\ &\quad \times \left[\sum_{n'} c_{n'}^* \exp\left(\frac{-2\pi i n'}{P}\left[\frac{\beta + \beta'}{2} y + \alpha'\right]\right)\right] \mathrm{d}y. \end{aligned}$$

All of the terms for which $n \neq n'$ are zero, so the integral becomes

$$K_S(\alpha,\beta,\alpha',\beta') = \frac{XY}{4} + \frac{X}{8} \mathrm{sinc}[N_x(\beta - \beta')] \frac{Y(\beta + \beta')}{2P} \times \int_{-P/(\beta+\beta')}^{P/(\beta+\beta')} \sum_n |c_n|^2 \exp\left(\frac{2\pi i n}{P}[\alpha - \alpha']\right) \mathrm{d}y.$$

Evaluating the integral,

$$K_S(\alpha,\beta,\alpha',\beta') = \frac{XY}{4} + \frac{XY}{8} \mathrm{sinc}[N_x(\beta - \beta')] \times \sum_{n=-\infty}^{\infty} |c_n|^2 \exp\left(\frac{2\pi i n}{P}[\alpha - \alpha']\right).$$

The sum is just the Fourier series of the autocorrelation of $B(y)$, represented by $B_A(y)$:

$$K_S(\alpha,\beta,\alpha',\beta') = \frac{XY}{4}\left(1+\frac{1}{2}\mathrm{sinc}[N_x(\beta-\beta')]B_A(\alpha-\alpha')\right). \tag{A3}$$

Equation (A3) describes the point spread function at projective coordinates (α,β) due to an impulse at (α',β'). The SVD can be found by solving the eigenvalue equation

$$\lambda_{mn}^2 F(\alpha',\beta') = \int_0^1\int_{-\infty}^{\infty} F_{mn}(\alpha,\beta)K(\alpha,\beta,\alpha',\beta')\mathrm{d}\alpha\mathrm{d}\beta \tag{A4}$$

with the eigenvectors being the singular vectors of the kernel and the eigenvalues being the squares of the singular values λ_{mn}. For simplicity, we assume the object is periodic such that $F(\alpha,\beta) = F(\alpha+P,\beta+1)$. An ansatz for the form of the singular vectors is

$$F_{mn}(\alpha,\beta) = e^{-2\pi i\left(\frac{\alpha m}{P}+\beta n\right)}.$$

Inserting this into the eigenvalue Eq. (A4),

$$\lambda_{mn}^2 e^{-2\pi i\left(\frac{\alpha' m}{P}+\beta' n\right)} = \frac{1}{P}\int_{-P/2}^{P/2}\mathrm{d}\alpha\int_0^1 \mathrm{d}\beta e^{-2\pi i\left(\frac{\alpha m}{P}+\beta n\right)}K(\alpha,\beta,\alpha',\beta').$$

On the right-hand side, the integrals over the first term in $K(\alpha,\beta,\alpha',\beta')$ evaluate to

$$\frac{XY}{4P}\int_{-P/2}^{P/2}\mathrm{d}\alpha e^{-\frac{2\pi i\alpha m}{P}}\int_0^1 \mathrm{d}\beta e^{-2\pi i\beta n} = \frac{XY}{4}\delta_{n0}\delta_{m0}.$$

The second term in K produces

$$\frac{XY}{8P}\int_{-P/2}^{P/2}\mathrm{d}\alpha e^{-\frac{2\pi i\alpha m}{P}}B_A(\alpha - \alpha')\int_0^1 \mathrm{d}\beta e^{-2\pi i\beta n}\,\mathrm{sinc}[N_x(\beta-\beta')].$$

The first integral evaluates to $(XY/8)\exp(-2\pi i m\alpha'/P)|c_m|^2$. For the second integral, since $N_x \gg 1$ the sinc function only contributes when $\beta \approx \beta'$ and we can extend the limits to $\pm\infty$. The result is the Fourier transform of the sinc, or $\exp(-2\pi\beta' n)\mathrm{rect}(n/N_x)/N_x$. We find singular values

$$\lambda_{mn} = \frac{\sqrt{XY}}{2}\sqrt{\delta_{m0}\delta_{n0} + \frac{|c_m|^2}{2N_x}\,\mathrm{rect}\left(\frac{n}{N_x}\right)}. \tag{A5}$$

To evaluate c_m, note that the function $B(y)$ is the convolution of the code sequence $a(y) = \sum_{n=0}^{N_y-1} a_n\delta(y - nP/N_y)$ and the pulse train $b(y) = \sum_{m=-\infty}^{\infty}\mathrm{rect}[N_y(y/P - m)]$, where N_y is the code length. From the convolution theorem, the continuous Fourier transform of $B(y)$ is $\tilde{B}(\nu') = \tilde{a}(\nu')\tilde{b}(\nu')$, where ν' is a spatial frequency and

$$\tilde{a}(\nu') = \int_{-\infty}^{\infty}\mathrm{d}y e^{-2\pi i y\nu'}a(y) = \sum_{n=0}^{N-1} a_n e^{-2\pi i n\nu' P/N_y}$$

$$\tilde{b}(\nu') = \int_{-\infty}^{\infty}\mathrm{d}y e^{-2\pi i y\nu'}b(y) = \frac{1}{N_y}\mathrm{sinc}\left(\frac{\nu' P}{N_y}\right)\sum_{m=-\infty}^{\infty}\delta\left(\nu' - \frac{m}{P}\right).$$

The coefficients c_m can be extracted via

$$c_m = \lim_{\epsilon\to 0}\int_{m/P-\epsilon}^{m/P+\epsilon}\mathrm{d}\nu'\tilde{B}(\nu') = \frac{1}{N_y}\mathrm{sinc}\left(\frac{m}{N_y}\right)\sum_{n=0}^{N_y-1} a_n e^{-2\pi i n m/N_y} = \frac{1}{N_y}\mathrm{sinc}\left(\frac{m}{N_y}\right)\tilde{a}_m,$$

where $\{\tilde{a}_m\}$ is the DFT of $\{a_n\}$. From Parseval's theorem, the RMS value of $\tilde{a}_m$ is

$$\sqrt{\frac{1}{N_y}\sum_{m=0}^{N_y-1}|\tilde{a}_m|^2} = \sqrt{\sum_{m=0}^{N_y-1}|a_n|^2} = \sqrt{N_y},$$

where the last line follows from $a_n = \pm 1$. Therefore, we have $|c_m| \approx \mathrm{sinc}(m/N_y)/\sqrt{N_y}$. Substituting this value for c_m in Eq. (A5), the singular values for $m \neq 0$ or $n \neq 0$ are

$$\lambda_{mn} = \frac{1}{2}\sqrt{\frac{XY}{N_x N_y}}\mathrm{rect}\left(\frac{n}{N_x}\right)\mathrm{sinc}\left(\frac{m}{N_y}\right).$$

This spectrum has maximum value $\lambda_{00} = \sqrt{XY}/2$ and roughly $N_x N_y$ singular values that are smaller by a factor of $\sqrt{N_x N_y}$. When estimating N^2 object coefficients with $N_x = N_y = N$, the singular values have magnitude proportional to $1/N$.

This work was supported by the Department of Homeland Security, Science and Technology Directorate through contract HSHQDC-11-C-00083.

References

1. K. MacCabe, K. Krishnamurthy, A. Chawla, D. Marks, E. Samei, and D. Brady, "Pencil beam coded aperture x-ray scatter imaging," Opt. Express **20**, 16310–16320 (2012).
2. K. MacCabe, A. Holmgren, M. Tornai, and D. Brady, "Snapshot 2D tomography via coded aperture x-ray scatter imaging," Appl. Opt. **52**, 4582–4589 (2013).
3. P. G. Lale, "The examination of internal tissues, using gamma-ray scatter with a possible extension to megavoltage radiography," Phys. Med. Biol. **4**, 159–167 (1959).
4. G. Harding and E. Harding, "Compton scatter imaging: a tool for historical exploration," Appl. Radiat. Isot. **68**, 993–1005 (2010).
5. T. T. Truong and M. K. Nguyen, "Radon transforms on generalized cormacks curves and a new compton scatter tomography modality," Inverse Probl. **27**, 125001 (2011).

6. F. T. Farmer and M. P. Collins, "A further appraisal of the compton scattering method for determining anatomical cross-sections of the body," Phys. Med. Biol. **19**, 808–818 (1974).
7. C. A. Carlsson, "Imaging modalities in x-ray computerized tomography and in selected volume tomography," Phys. Med. Biol. **44**, R23 (1999).
8. M. T. E. Golay, "Multi-slit spectrometry," J. Opt. Soc. Am. **39**, 437 (1949).
9. L. Mertz, *Transformations in Optics* (Wiley, 1965), Vol. **1**.
10. M. Harwit and N. J. Sloane, *Hadamard Transform Optics* (Academic, 1979), Vol. **1**.
11. S. R. Gottesman and E. E. Fenimore, "New family of binary arrays for coded aperture imaging," Appl. Opt. **28**, 4344–4352 (1989).
12. D. J. Brady, *Optical Imaging and Spectroscopy* (Wiley-OSA, 2009).
13. A. Wagadarikar, R. John, R. Willett, and D. J. Brady, "Single disperser design for coded aperture snapshot spectral imaging," Appl. Opt. **47**, B44–B51 (2008).
14. A. Mrozack, D. L. Marks, and D. J. Brady, "Coded aperture spectroscopy with denoising through sparsity," Opt. Express **20**, 2297–2309 (2012).
15. B. R. Frieden, "Band-unlimited reconstruction of optical objects and spectra," J. Opt. Soc. Am. **57**, 1013–1019 (1967).
16. S. W. Golomb and G. Gong, *Signal Design for Good Correlation: For Wireless Communication, Cryptography, and Radar* (Cambridge University, 2005).
17. P. Boccacci and M. Bertero, *Introduction to Inverse Problems in Imaging* (Institute of Physics, 1998).
18. D. Slepian, "Prolate spheroidal wave functions, Fourier analysis, and uncertainty—I," Bell Syst. Tech. J. **40**, 43–63 (1961).